Photoinduced structural recovery dynamics of rare-earth nickelate thin films

Jugal Mehta, Scott Smith, Jianheng Li, Kenneth Ainslie, Nadia Albayati, Toyanath Joshi, Pooja Rao, Yu-Hsing Cheng, Spencer Jeppson, Rahul Jangid, Evguenia Karapetrova, Donald A. Walko, Haidan Wen, David Lederman, and Roopali Kukreja

Phys. Rev. Materials **7**, 096201 — Published 7 September 2023

DOI: 10.1103/PhysRevMaterials.7.096201

Photoinduced structural recovery dynamics of rare-earth nickelate thin films

Jugal Mehta,[1] Scott Smith,[1] Jianheng Li,[1] Kenneth Ainslie,[1] Nadia Albayati,[1] Toyanath Joshi,[2] Pooja Rao,[1] Yu-Hsing Cheng,[1] Spencer Jeppson,[1] Rahul Jangid,[1] Evguenia Karapetrova,[3] Donald A. Walko,[3] Haidan Wen,[3] David Lederman,[2] and Roopali Kukreja[1]

[1] *Department of Materials Science and Engineering, University of California Davis, Davis, California 95616, USA*
[2] *Department of Physics, University of California Santa Cruz, Santa Cruz, California 95064, USA*
[3] *Advanced Photon Source, Argonne National Laboratory, Lemont, Illinois 60439, USA*

(Dated: August 16, 2023)

Photoinduced structural dynamics of rare-earth nickelate thin films, $NdNiO_3$ and $SmNiO_3$, grown on (001) oriented $SrTiO_3$ were studied using time-resolved x-ray diffraction. The evolution of the (002) Bragg peak was tracked following laser excitation. The recovery pathways were found to be strongly dependent on laser fluence for $NdNiO_3$ and distinct for the two rare-earth nickelates. The recovery of the (002) peak shifts was modeled using a one-dimensional thermal diffusion model which showed that the recovery processes are non-thermal at high fluences. For $NdNiO_3$, the timescales for the recovery of the (002) peak shift were found to be closely related to Ni magnetism recovery, potentially indicating magneto-structural coupling. Moreover, the evolution of integrated intensity and full-width-half-maximum points towards the presence of a structural phase separation during recovery. Our studies highlight structural recovery pathways in nickelates by comparing the distinct responses of the photoinduced metal-insulator transition in $NdNiO_3$ and $SmNiO_3$.

I. INTRODUCTION

Photoexcitation by means of ultrashort optical laser pulses provides a novel approach to initiate and manipulate an insulator-to-metal transition (IMT) in transition metal oxides [1–5]. In comparison to other methods of controlling IMT such as epitaxial strain [6, 7], doping [8, 9], magnetic field [10, 11] or applied voltage [12, 13], photoexcitation provides a unique way to identify the interplay of electronic, magnetic and structural degrees of freedom in time domain. It also enables access to transient metastable states not observed in thermal equilibrium [14]. Recently, it has been shown that the photoinduced IMT in rare-earth nickelates ($RNiO_3$ where R= Nd, Pr, Sm, Eu, etc.) can be driven at subpicosecond timescales with a laser fluence nearly an order of magnitude smaller than the widely studied vanadate system [15, 16]. Additionally, the IMT can be tuned to near room temperature via substrate strain [6], substrate symmetry [17] or by choice of rare-earth cation [18], making rare earth nickelates excellent candidates for ultrafast manipulation.

$RNiO_3$ undergo a metal-to-insulator transition (MIT) on cooling during which the crystal structure transforms from orthorhombic (P_{bnm}) to monoclinic ($P_{2_1/c}$), the paramagnetic state switches to an antiferromagnetic state and charge ordering occurs [18–20]. In $RNiO_3$, the magnetic and electronic properties can be tuned by varying the tolerance factor of the perovskite structure. A smaller rare earth cation leads to a more distorted structure, resulting in a 500 K variation of the transition temperature (T_{MIT}) as the rare earth cation size decreases from Pr to Lu for bulk nickelates [18]. For $NdNiO_3$, the T_{MIT} and Neel temperature (T_N) coincide while nickelates with smaller rare-earth cations such as $SmNiO_3$ (SNO) show a separation of the electronic and magnetic transition with $T_{MIT} > T_N$. Heteroepitaxial strain results in separation of the insulator-to-metal and the magnetic phase transition temperature observed in bulk NNO, and compressive strain can lead to disappearance of the MIT, resulting in metallic films over the entire temperature range [6]. As epitaxial strain or rare earth cation can significantly alter the phase diagram, photoinduced measurements of the nickelate family can provide unique insights into the coupling of electronic, magnetic and structural degrees of freedom as well as methods to tailor ultrafast behavior.

In this article, we have utilized time-resolved x-ray diffraction (tr-XRD) to study the photoinduced structural recovery dynamics of tensile strained NNO and $SmNiO_3$ (SNO) thin films. While extensive work has been performed on understanding excitation pathways from the insulating to the metallic state[16, 21–29], only a few studies have focused on the recovery pathways from the metallic to insulating state in nickelates [15]. Our tr-XRD experiments for NNO revealed a strong laser fluence dependence for structural recovery indicating presence of non-thermal pathways at higher fluence. The sign of Bragg peak shifts for both NNO and SNO are consistent with thermal diffusion model calculations. Photoinduced strain recovery in NNO occurs at similar timescales as Ni magnetism [26], indicating magneto-structural pathways for recovery. Measurement of the full-width-half-maximum and integrated intensity of the (002) Bragg peak suggests structural phase separation, which is consistent with recent reports for NNO [15]. Phase separation is not observed for SNO, highlighting the distinct response of two nickelates with different rare-earth cations. The coupling of structural recovery with magnetism as well as domain dynamics at ultrafast timescales reveals the rich transient physics observed in rare-earth nickelates.

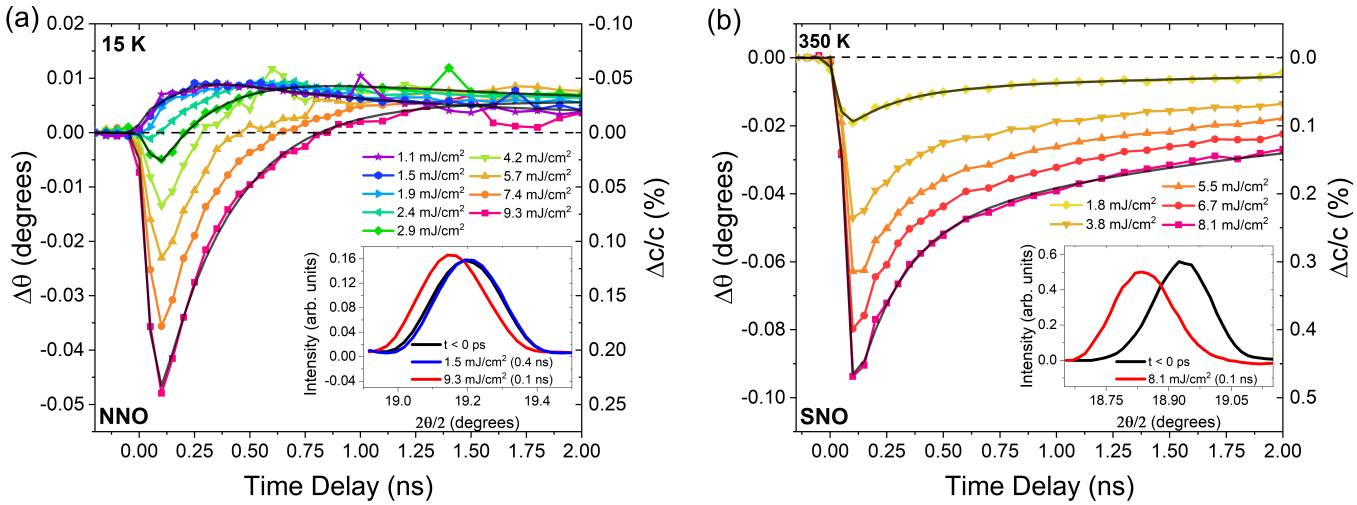

FIG. 1. Photoinduced structural evolution of NNO and SNO thin films: (a) NNO (002) peak shift as a function of time delay for different incident pump fluences. The inset shows NNO (002) Bragg peak at 100 ps after photoexcitation for a fluence of 9.3 mJ/cm^2 (red) and 400 ps for a fluence of 1.5 mJ/cm^2 (blue) which are compared with the Bragg peak before laser excitation (black). For the low fluence, the peak shift indicates a lattice contraction which reaches its maximum value at 400 ps, while for the higher fluence, the peak shift shows a lattice expansion which reaches its maximum value at 100 ps. (b) SNO (002) peak shift as a function of time delay for different incident pump fluences. The inset shows SNO (002) Bragg peak before photoexcitation (black) and at 100 ps for a laser fluence of 8.1 mJ/cm^2 (red). The SNO peak shift shows an out-of-plane expansion of the lattice within 100 ps. Black lines overlaid on the delay curves represent exponential fits as described in the text.

II. EXPERIMENTAL METHODS

A NNO thin film (19 nm) was deposited on a (001) oriented $SrTiO_3$ (STO) substrate using RF magnetron sputtering in a 3:1 Ar/O_2 environment and a total pressure of 130 mTorr at 500° C. A SNO thin film (30 nm) was deposited on a (001) oriented STO substrate using pulsed laser deposition [30]. Reciprocal space maps around the (103) peaks confirmed that both films are commensurate with the substrate. Note that psuedocubic notation is used throughout the article for Miller indices. The STO substrate imparts a heteroepitaxial tensile strain of 2.6% and 2.7% for the NNO and SNO film, respectively. $\theta-2\theta$ scans of the (002) Bragg peak show that the out-of-plane lattice parameter of NNO and SNO thin films is 3.778 Å and 3.816 Å at 300 K, respectively. Resistivity measurements indicate T_{MIT} of 106 K for NNO and above 400 K for SNO (see Section S1 of the Supplemental Material [31]). The variation in T_{MIT} of these films compared to literature could be due to oxygen deficiencies caused due to high tensile strain. The temperature dependent x-ray diffraction (XRD) data on NNO and SNO were collected at Sector 33 at the Advanced Photon Source (APS) with an x-ray energy of 16 keV and will be discussed below in Section IV.

Tr-XRD measurements were performed at Sector-7 at APS at Argonne National Laboratory. Laser pulses with 60 fs pulse width ('pump') from a Ti:Sapphire laser system (repetition rate 1 kHz) were used to induce the IMT. The pump wavelength (800 nm) is above the band gap of NNO and SNO. The laser fluence are reported in terms of the incident fluence. The photoinduced structural changes were measured using x-ray pulses tuned to 10 keV ('probe'). The x-ray spot size was 50 µm and 100 µm for NNO and SNO, respectively, and the laser spot size was 500 µm. Tr-XRD measurements were performed at (002) and $(\frac{1}{2}\frac{\bar{1}}{2}\frac{3}{2})$ Bragg peaks for a delay range of -0.2 ns to 6 ns for NNO and -0.15 ns to 10 ns for SNO. Diffracted x-ray photons were collected by a two-dimensional pixel array detector (Pilatus 100K, Dectris Ltd.) with a pixel size of 172 µm. $\theta-2\theta$ scans of the (002) Bragg peak and L-scans of the $(\frac{1}{2}\frac{\bar{1}}{2}\frac{3}{2})$ taken at specific time-delays after laser excitation were fit with a Gaussian curve to extract peak position and full-width-half-maximum (FWHM) of the peak. Area under the curve was calculated to obtain the integrated intensity. Note that the presence of twinned orthorhombic domains in NNO/STO films can also contribute to the intensity of half order Bragg peak [36]. Photoinduced change in these parameters are plotted relative to the before time zero value throughout the article.

III. EXPERIMENTAL RESULTS

Figure 1 shows the (002) peak shift ($\Delta\theta$) for NNO and SNO films following photoexcitation for a range of pump laser fluences. NNO was photoexcited from its antiferromagnetic insulating phase at 15 K whereas SNO was photoexcited from its paramagnetic insulating phase at

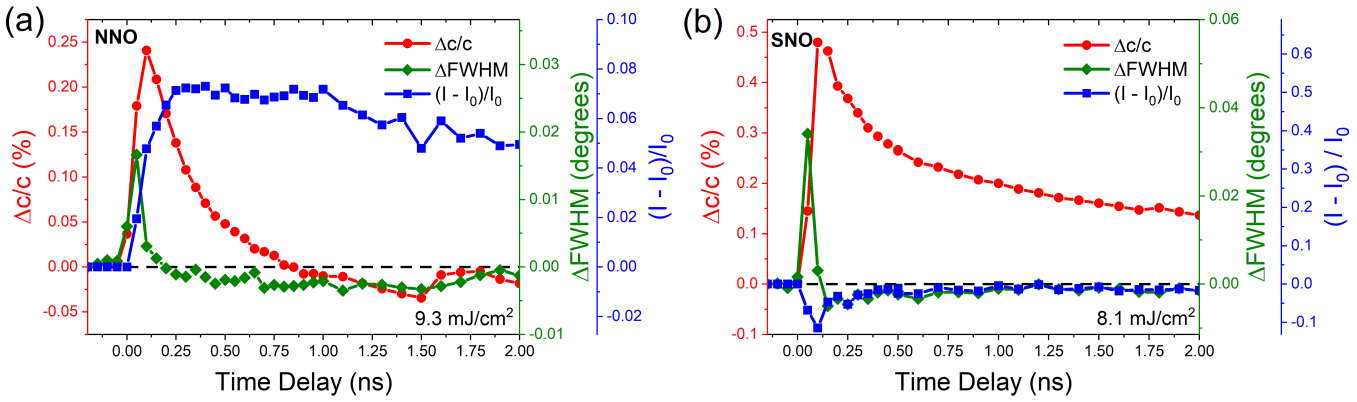

FIG. 2. Comparison of photoinduced strain (red circles), FWHM (green diamonds) and integrated intensity (blue squares) for (002) Bragg peak for (a) NNO film for a pump fluence of 9.3 mJ/cm^2, and (b) SNO film for a pump fluence of 8.1 mJ/cm^2.

350 K. A clear sign reversal of the photoinduced peak shift with increasing laser fluence is observed for NNO in Figure 1(a). For 1.1 - 1.9 mJ/cm^2, a positive $\Delta\theta$ indicating a decrease in c-lattice parameter is observed. While above 2.4 mJ/cm^2, a negative $\Delta\theta$ indicating an increase in the c-lattice parameter is measured. The inset in Figure 1(a) shows NNO (002) Bragg peak for pump fluence of 1.5 mJ/cm^2 at 400 ps and 9.3 mJ/cm^2 at 100 ps. The comparison with Bragg peak before photoexcitation clearly shows the shift in opposite directions for the two pump fluences. For SNO, all fluences result in a photoinduced peak shift towards lower theta values indicating expansion along c-axis as shown in Figure 1(b). The inset in Figure 1(b) shows SNO (002) Bragg peak for pump fluence of 8.1 mJ/cm^2 at 100 ps.

The photoinduced evolution of the (002) Bragg peak was fit using an exponential function as described in Section S3 of SM [31]. The results of the temporal fits are shown in Figure 1(a, b) (black curves) and time constants are tabulated in Table S1 in SM [31]. For NNO, the peak shift dynamics can be separated into three fluence regimes: low, intermediate and high fluence regime. In the low fluence regime (1.1 - 1.9 mJ/cm^2), the laser excitation leads to a positive $\Delta\theta$ (τ_1) which reaches a maximum value within 400 ps after which it starts to recover (τ_2). The time constants $\tau_1 \sim 150$ ps and $\tau_2 \sim 1-2$ ns are similar for all fluences in the low fluence regime. In the intermediate fluence regime (2.4 - 4.2 mJ/cm^2), the laser excitation leads to a negative $\Delta\theta$ within <100 ps, limited by the temporal resolution of the experiment. An initial quick recovery ($\tau_1 \sim 200$ ps) results in $\Delta\theta$ crossing zero and becoming positive followed by a longer recovery ($\tau_2 \sim 1-2$ ns). For the high fluence regime (5.7 - 9.3 mJ/cm^2), an immediate negative $\Delta\theta$ (<100 ps) succeeded by a quick recovery (τ_1) which results in overshooting the initial ground state followed by a slow recovery is observed. For high fluence regime, τ_1 shows a fluence dependence and increases from 240 ps $\pm$ 20 ps to 320 ps $\pm$ 20 ps for 5.7 mJ/cm^2 to 9.3 mJ/cm^2. Following the initial quick recovery, the value of $\Delta\theta$ remains almost constant within the measured range of 6 ns, indicating a longer recovery compared to intermediate and low fluences. In comparison, the photoinduced evolution for SNO varies monotonically with the increasing laser fluence with no distinct fluence regimes. As shown in Figure 1(b) for SNO, an immediate negative $\Delta\theta$ is observed within 100 ps and the recovery processes consists of a quick recovery ($\tau_1 \sim 200$ ps) and a slow recovery ($\tau_2 \sim 2$ ns) for all the measured fluences.

In order to further investigate the photoinduced structural recovery, the (002) Bragg peak was fit with a Gaussian profile to obtain integrated intensity and FWHM, which are related to changes in crystal symmetry and crystallite size respectively. Figure 2 compares the temporal evolution of out-of-plane strain, FWHM and integrated intensity for (002) Bragg peak for the highest fluence measured for both NNO and SNO thin films (Other fluences are presented in Section S4 of SM[31]). A clear difference between temporal evolution of strain, FWHM and integrated intensity is observed for both thin films, indicating the presence of multiple processes during recovery. For NNO, the FWHM achieves a maximum value at $\approx$ 50 ps, whereas the strain shows a maximum at $\approx$ 100 ps. While the 50 - 100 ps pulse width of synchrotron x-rays limits insight into this decoupling during excitation, it provides information regarding recovery processes. The FWHM overshoots initial value during the quick recovery resulting in a sign reversal which recovers slowly to the initial state. On the other hand, the integrated intensity shows a continuous increase followed by a slower decay to the initial state. For SNO, both the FWHM and integrated intensity show a different temporal evolution compared to NNO. After laser excitation, fast modification is observed for both FWHM and integrated intensity, which recovers within $\sim$ 250 ps to the initial state.

We also measured the half order peak ($\frac{1}{2}\frac{\overline{1}}{2}\frac{3}{2}$) for NNO and ($\frac{\overline{1}}{2}\frac{1}{2}\frac{3}{2}$) for SNO (Section S5 and S6 of the SM [31] respectively.) , which arises due to octahedral rotations in the perovskite structure [37]. Similar to (002) peak,

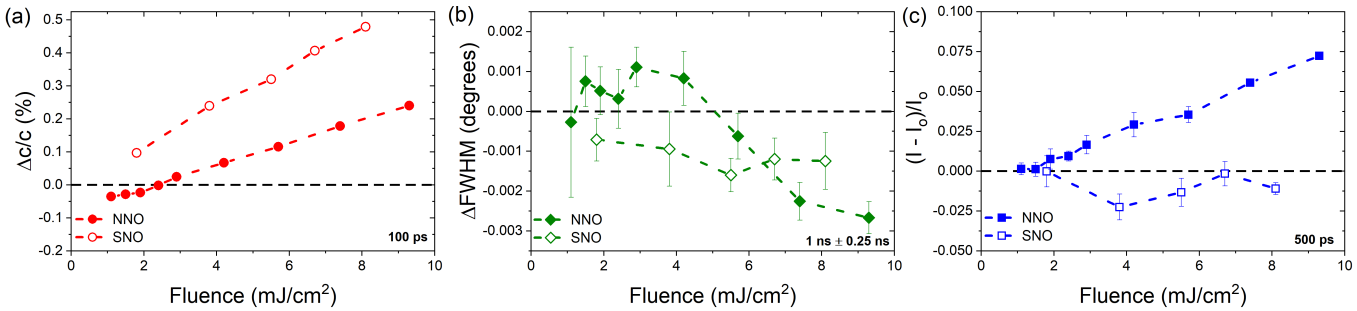

FIG. 3. Fluence dependence of strain, FWHM and integrated intensity: (a) Photoinduced changes in out-of-plane strain of NNO (closed red circles) and SNO (open red circles) at 100 ps as a function of laser fluence. Error bars are on the order of symbol size for strain. (b) Photoinduced change in (002) FWHM of NNO (closed green diamonds) and SNO (open green diamonds) as a function of laser fluence. An average of FWHM in the time delay range of 0.75 ns - 1.25 ns is shown with error bars representing standard deviation. (c) Photoinduced change in (002) integrated intensity of NNO (closed blue squares) and SNO (open blue squares) at 500 ps as a function of laser fluence. Error bars represent standard deviation of integrated intensity before laser excitation.

a shift to higher L is observed for low fluences whereas high fluences cause a shift to lower L. On the other hand, no photoinduced change in peak position, FWHM or integrated intensity was observed in the h-direction, indicating that epitaxial strain from the substrate effectively pins the in-plane lattice parameters of the film.

Figure 3 shows the fluence dependence for strain, FWHM and integrated intensity of the (002) Bragg peak. The comparison of photoinduced strain for NNO and SNO thin films at 100 ps clearly shows non-linear and linear fluence dependence, respectively. The sign reversal in strain for NNO is similar to temperature dependent static XRD which will be discussed in Section IV. Figure 4(b) presents an average FWHM value for a time delay range of 1 ns $\pm$ 0.25 ns. For NNO, no significant change in FWHM is observed for the low and intermediate fluence regime whereas a decrease in the FWHM is seen in the high fluence regime. For SNO, no fluence dependence of FWHM is detected. Figure 3(c) plots the integrated intensity at 500 ps for NNO and SNO. For NNO, no significant change is observed for the low fluence regime, while a linear fluence dependence is observed for intermediate and high fluence regime. This linear increase in integrated intensity is higher than the calculate increase of 0.01% due to change in crystal symmetry from monoclinic ($P2_1/n$) to orthorhombic (Pbnm) crystal structure using atomic positions reported in Garcia-Munoz et al. [20]. In contrast, no significant change in integrated intensity is observed for SNO. The striking differences in fluence dependence of NNO and SNO indicate towards different recovery processes at play for the two nickelate systems. Thermal modeling and analysis was performed to further discern the recovery processes underlying the structural evolution in nickelate thin films.

IV. THERMAL MODEL AND ANALYSIS

A one-dimensional thermal diffusion equation of a heterostructure was solved numerically to generate a film temperature vs time profile (Section S8 of the SM [31]). Similar model has been previously utilized for complex oxides thin film heterostructures [38, 39]. While most sample parameters used in the model were obtained from literature, interface conductance, an important parameter in determining the cooling rate estimated by the thermal model, is not currently available for NNO/STO and SNO/STO. Thermal simulations were carried out for 1,000 W/cm^2/K and 100,000 W/cm^2/K to cover a range of values typically seen for oxides. For example, $SrRuO_3/SrTiO_3$ heterostructure has one of the highest reported values of interface conductance of 80,000 W/cm^2/K [40]. Higher interface conductivity value of 100,000 W/cm^2/K resulted in better fit of experimental data at lower and intermediate fluences (Fig S12 of SM), and thus was used for the simulations.

The temperature vs time curves obtained from the thermal diffusion model were converted to $\Delta\theta$ vs time delay by utilizing temperature-dependent XRD data measured in thermal equilibrium. Although, one important caveat is that during laser excitation the substrate remains near the ambient temperature (pump energy is below the band gap of STO), while in temperature-dependent XRD measurements both substrate and film are in thermal equilibrium. In order to address this difference, we modified temperature dependent XRD curve to include Poisson's expansion due to in-plane clamping of the film by the substrate (Section S8 of the Supplemental Material [31]). Figure 4(a) and (b) presents the (002) peak shift of NNO and SNO respectively, obtained using temperature dependent XRD measurements, as well as peak shift calculated after considering the in-plane epitaxial constraint imparted by the substrate. Note that peak shifts $\Delta\theta$ are plotted relative to the (002) peak posi-

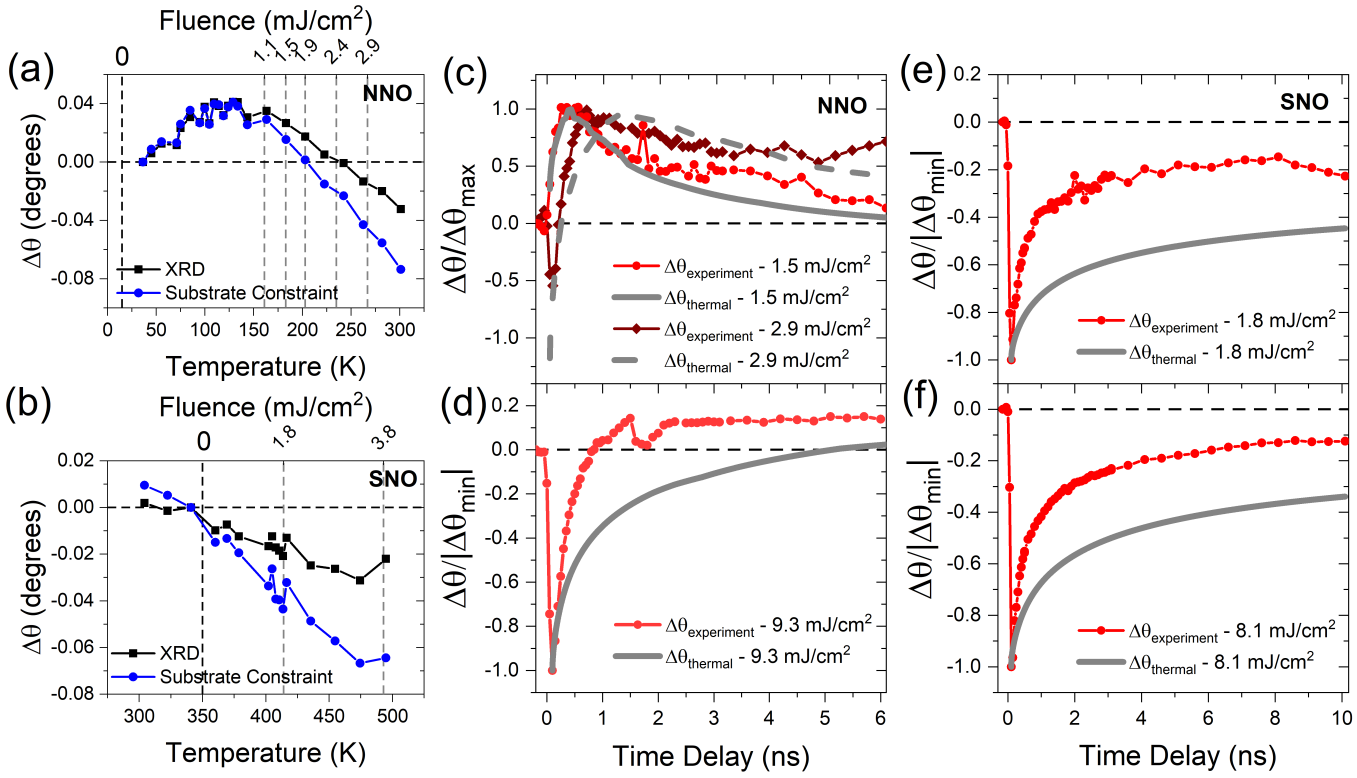

FIG. 4. Thermal diffusion modeling of NNO and SNO: Temperature dependence of (002) peak shift for (a) NNO and (b) SNO obtained from temperature dependent XRD measurements (black squares) and after including in-plane clamping by substrate (blue circles). Vertical dashed lines mark the initial film temperature achieved for respective pump fluence. Comparison of experimental and simulated NNO (002) peaks shift for pump fluence of (c) 1.5 mJ/cm^2 (circles) and 2.9 mJ/cm^2 (diamonds) and (d) 9.3 mJ/cm^2. Comparison of experimental and simulated SNO (002) peak shift for pump fluence of (e) 1.8 mJ/cm^2 and (f) 8.1 mJ/cm^2. Simulations were done for an interface conductance of 100,000 W/cm^2/K and assuming an initial sample temperature of 15 K and 350 K for NNO and SNO respectively, same as the experimental measurements.

tion at 30 K for NNO and 350 K for SNO. The measured XRD for NNO (black curve) shows that as the film is heated from its insulating state, $\Delta\theta$ increases until T_{IMT} is achieved, after which $\Delta\theta$ starts to decrease again, indicating contraction followed by expansion of the unit cell. This is consistent with the literature for films grown on STO [36]. The substrate constraint calculated peak shift (blue curve) also shows similar behavior albeit with larger magnitude due to in-plane epitaxial constraint. Considering substrate constraint for SNO leads to a larger negative $\Delta\theta$ i.e. expansion of the c-lattice parameter which increases with temperature. Note that while the temperature dependence of the lattice parameter for SNO thin films has not been reported in the literature, the c-lattice parameter of bulk SNO shows a change at the T^{MIT} similar to NNO. For films, the tensile in-plane strain from the substrate or the presence of oxygen vacancies could be responsible for differences in behavior compared to bulk.

Figure 4(c)-(f) compares the simulated peak shifts ($\Delta\theta_{\text{thermal}}$) with experimental peak shifts ($\Delta\theta_{\text{experiment}}$) for NNO and SNO. Note that $\Delta\theta_{\text{thermal}}$ and $\Delta\theta_{\text{experiment}}$ have been normalized for comparison. For the low and intermediate fluences, normalization was done using the maxima in the peak shift while for higher fluences and SNO, normalization was done using minima in the peak shift. Three key observations can be made from the calculated temperatures and simulated peaks shifts for NNO. Firstly, the lowest measured fluence of 1.1 mJ/cm^2 leads to a film temperature of 161 K, implying that laser excitation can drive the IMT even for the low fluence regime. The corresponding temperature for a given fluence is indicated in Fig 4(a). Secondly, the sign of experimentally observed peak shift for all fluences is reproduced by the model. Specifically, the thermal diffusion model and simulated peak shift can explain the photoinduced peak shift for low and intermediate fluences. As the film temperature is only slightly above T_{IMT} for low fluence regime, a positive photoinduced peak shift is observed for both experimental and simulated curves. During recovery as the temperature lowers, a maxima in $\Delta\theta$ is observed due to the inverted U-shape of temperature dependent XRD (Fig 4(a)). Increasing the fluence to intermediate regime leads to higher temperature which corresponds to negative $\Delta\theta$ consistent with temperature dependent XRD. During recovery, as the film temperature

lowers, $\Delta\theta$ traverses temperature dependent XRD which results in a sign reversal and a maxima in the peak shift again due to the inverted U-shape of the XRD. Note that the maxima in peak shift is the same for low and intermediate fluence regimes as the film reaches same structure dictated by temperature dependent XRD. Lastly, for high fluence regime, the simulated peak shift cannot reproduce experimentally observed behavior. However, the model correctly shows that the film does not cool fast enough to traverse the inverted U-shaped of temperature dependent XRD within the measured delay range, which is consistent with the experimental observation of no maxima observed in peak shift for the high fluence regime. The disparity between recovery timescales estimated by the thermal diffusion model and experiment increases with increasing laser fluence pointing towards non-thermal recovery behavior at higher fluences.

For SNO, experimentally observed negative peak shifts are consistent with simulated peak shifts. However, the simulated recovery rates of $\Delta\theta_{\text{thermal}}$ are slower than experimentally observed peak shifts $\Delta\theta_{\text{experiment}}$ even at lower fluences. The discrepancy between $\Delta\theta_{\text{thermal}}$ and $\Delta\theta_{\text{experiment}}$ could be due to additional factors not included in this simple model. For example, due to lack of materials parameters for SNO such as band gap and thermal conductivity, parameters of NNO were used. Furthermore, a Poisson's ratio of 0.3 was assumed for the calculations. Additionally, an assumption that heat capacity for bulk can be used for thin films can also potentially introduce errors in temperature estimates. Overestimation of temperature can also occur due to absence of latent heat term in the model. Additionally, limited temperature range of thermal XRD measurements implied that linear extrapolation was used to estimate peak shift at higher temperatures, which can overestimate the calculated peak shifts. Overall, these simulations suggest that while the sign of photoinduced structural changes seen in NNO and SNO is dictated by thermal transport, the role of non-thermal processes for high fluences cannot be ruled out due to limitations of the thermal model.

V. DISCUSSION

As mentioned above, the thermal diffusion model simulates major aspects of the recovery dynamics for low and intermediate fluences for NNO. However, the fast recovery of NNO (002) peak shift for the higher fluence regime cannot be reproduced by thermal diffusion model. Additionally, in the high fluence regime, the photoinduced increase in NNO (002) integrated intensity Bragg peak (Figure 2 and SM Figure S4) is higher than expected from structure factor calculations. Both the peak shift and integrated intensity behavior thus point towards non-thermal recovery in the high fluence regime.

We compared the structural dynamics measured in this article with recovery dynamics of magnetism [26] and conductivity [15] in NNO, reported in the literature for same excitation wavelength (800 nm) and laser fluences that led to comparable film temperatures. Ultrafast resonant soft x-ray magnetic scattering measurements of NNO conducted by Caviglia et al. [26] have shown that higher pump fluences (> 1 mJ/cm^2, excited from a temperature of 40 K) lead to a complete quenching of the antiferromagnetic order at the Ni site, which recovers with a time constant > 100 ps. Figure 5(a) compares the ultrafast evolution of Ni magnetism and the (002) peak shift for NNO and SNO. We see that the NNO peak shift recovers at similar timescales as that of Ni magnetism while SNO recovery is slower than NNO and Ni magnetism. Similar recovery timescales for structural Bragg peak and Ni magnetism point towards magneto-structural coupling which has been reported to play a major role in driving photoinduced IMT in NNO [16]. On the other hand, while the recovery of SNO peak shift is slower than that of NNO, direct measurements of Ni magnetism dynamics in SNO below Neel temperature are required to conclusively understand the role of magnetism on the photoexcited structural dynamics in nickelates. Additionally, structural measurements at ultrafast timescales (1-100 ps) could provide further insights into coupling of magnetism, electronic and structural degrees of freedom.

Figure 5(b) compares the evolution of (002) integrated intensity measured in our study with the ultrafast THz conductivity behavior of NNO [15]. The slow non-exponential recovery observed in the THz conductivity dynamics was attributed to nucleation and growth of the insulating domains from the metallic domains as the film cools below T_{MIT}. The striking similarity in the recovery profiles points towards a similar process at play. This phase separated and heterogeneous excited state can result in strain gradients and mosaicity in the film. Mosaicity arising due to strain gradients can result in integrated intensity variations [41, 42]. On the other hand, no such increase in integrated intensity is observed for SNO. While THz conductivity studies of SNO are not yet available in literature, THz conductivity of $EuNiO_3$, which also has a smaller tolerance factor than NNO and displays a seperation in T_{MIT} and T_N similar to SNO, shows an exponential recovery due to the absence of nucleation and growth [15]. The resultant system would have minimal strain gradient and could be a reason for no observed variation in integrated intensity at > 250 ps timescales. X-ray microscopy studies at ultrafast timescales would be important to uncover the spatial heterogeneity of this transition in nickelates at the nanoscale.

VI. CONCLUSION

In summary, we performed a comprehensive study of structural dynamics in rare-earth nickelate thin films as a function of pump fluences. The photoinduced behavior of the out-of-plane lattice parameter shows a distinct response for NNO and SNO which was explained

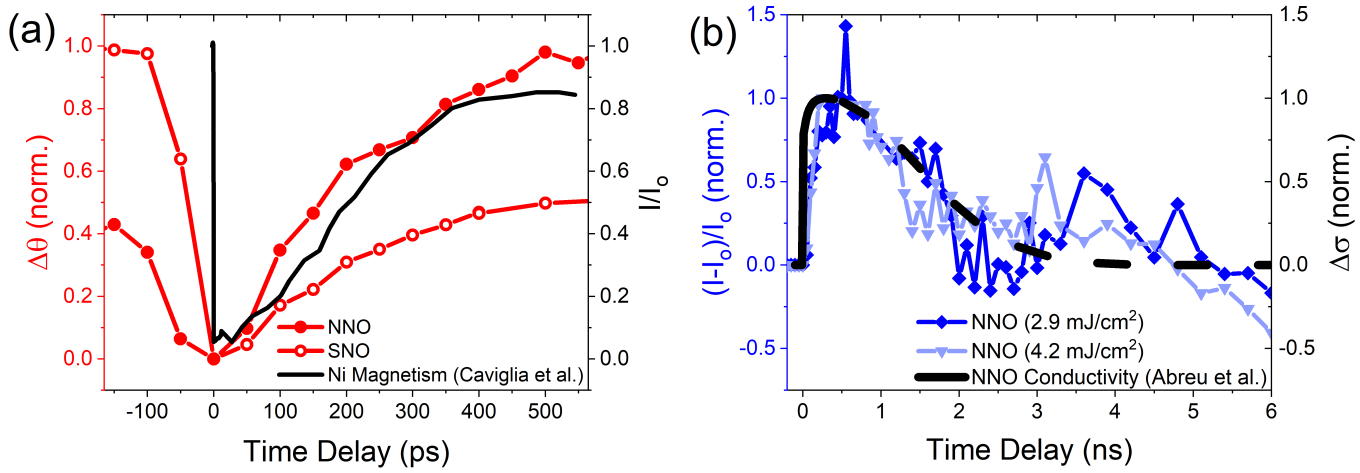

FIG. 5. Comparison of photoinduced recovery of structural (this article), magnetic [26] and electronic degrees of freedom [15]: (a) Comparison of the (002) peak shift for NNO and SNO observed in our study with Ni magnetism dynamics reported by Caviglia et al. [26] for NNO. Black curve represents Ni magnetism following photoexcitation of NNO from 40 K with a laser fluence of 2.7 mJ/cm^2 which is compared with the (002) peak shift of NNO from 15 K (closed red circles) and SNO from 350 K (open red circles) with a laser fluence of 2.9 mJ/cm^2 and 3.8 mJ/cm^2 respectively. (b) Comparison of NNO (002) integrated intensity with the ultrafast THz conductivity dynamics of NNO reported by Abreu et al. [15]. The black curve represents the THz conductivity of NNO measured at 103 K following photoexcitation with laser fluence of 1.5 mJ/cm^2 which is compared with the change in integrated intensity for NNO measured at 15 K with a laser fluence of 2.9 mJ/cm^2 (blue diamonds) and 4.2 mJ/cm^2 (light blue inverted triangles). Dashed black lines for conductivity are generated from equation of fit provided in reference [15]. Note that curves are normalized to compare recovery timescales.

using a one-dimensional thermal diffusion model. The photoinduced recovery of the out of plane lattice parameter occurs at similar timescales as that of ultrafast Ni magnetism, hinting towards magneto-structural coupling at ultrafast timescales. The integrated intensity and FWHM capture indications of a photoinduced phase separation in NNO that is absent for SNO, implying that the first order nature of MIT of NNO is manifested in ultrafast processes. Overall, the decoupling of recovery timescales for photoinduced strain and integrated intensity points towards a thermally inaccessible structural state with complex recovery pathways where the system is phase-separated into metallic and insulating domains, and magnetism is potentially linked to the photoinduced strain. These insights improve our understanding of the recovery mechanisms of the lattice and its interactions with multiple degrees of freedom at nanosecond timescales and nano- to meso- lengthscales, which can help facilitate faster magnetic and electronic switching.

VII. ACKNOWLEDGEMENTS

We thank Prof. Paul Evans and Sangeeta Rajpurohit for fruitful discussions on temporal dynamics of nickelates. This work was supported by National Science Foundation (DMR-1902652). This research used resources from the Advanced Photon Source, a US Department of Energy (DOE) Office of Science User Facilities operated for the DOE Office of Science by Argonne National Laboratory (under contract No. DE-AC02-06CH11357).

[1] M. Fiebig, K. Miyano, Y. Tomioka, and Y. Tokura, Visualization of the local insulator-metal transition in $Pr_{0.7}Ca_{0.3}MnO_3$, Science **280**, 1925 (1998).
[2] A. Cavalleri, C. Tóth, C. W. Siders, J. A. Squier, F. Ráksi, P. Forget, and J. C. Kieffer, Femtosecond structural dynamics in VO_2 during an ultrafast solid-solid phase transition, Physical Review Letters **87**, 237401 (2001).
[3] A. Tomeljak, H. Schäfer, D. Städter, M. Beyer, K. Biljakovic, and J. Demsar, Dynamics of photoinduced charge-density-wave to metal phase transition in $K_{0.3}MoO_3$, Physical Review Letters **102**, 066404 (2009).
[4] V. R. Morrison, R. P. Chatelain, K. L. Tiwari, A. Hendaoui, A. Bruhács, M. Chaker, and B. J. Siwick, A photoinduced metal-like phase of monoclinic VO_2 revealed by ultrafast electron diffraction, Science **346**, 445 (2014).
[5] S. De Jong, R. Kukreja, C. Trabant, N. Pontius, C. Chang, T. Kachel, M. Beye, F. Sorgenfrei, C. Back, B. Bräuer, *et al.*, Speed limit of the insulator–metal transition in magnetite, Nature Materials **12**, 882 (2013).
[6] J. Liu, M. Kargarian, M. Kareev, B. Gray, P. J. Ryan, A. Cruz, N. Tahir, Y.-D. Chuang, J. Guo, J. M.

Rondinelli, *et al.*, Heterointerface engineered electronic and magnetic phases of $NdNiO_3$ thin films, Nature Communications **4**, 1 (2013).

[7] S. Catalano, M. Gibert, V. Bisogni, O. Peil, F. He, R. Sutarto, M. Viret, P. Zubko, R. Scherwitzl, A. Georges, *et al.*, Electronic transitions in strained $SmNiO_3$ thin films, APL Materials **2**, 116110 (2014).

[8] A. Maignan, F. Damay, C. Martin, and B. Raveau, Nickel-induced metal-insulator transition in the small a cation manganites $Ln_{0.5}Ca_{0.5}MnO_3$, Materials Research Bulletin **32**, 965 (1997).

[9] M. Melo Jorge, M. Nunes, R. Silva Maria, and D. Sousa, Metal-insulator transition induced by Ce doping in $CaMnO_3$, Chemistry of Materials **17**, 2069 (2005).

[10] Y. Hideki, K. Hazuki, T. Yasuhide, and T. Yoshinori, Magnetic-Field-Induced Metal-Insulator Transition in $Pr_{0.7}Ca_{0.3}MnO_3$, Journal of the Physical Society of Japan **65**, 1043 (1996).

[11] Y. Tomioka, A. Asamitsu, H. Kuwahara, Y. Moritomo, M. Kasai, R. Kumai, and Y. Tokura, Magnetic-field-induced metal-insulator transition in perovskite-type manganese oxides, Physica B: Condensed Matter **237**, 6 (1997).

[12] J. del Valle, Y. Kalcheim, J. Trastoy, A. Charnukha, D. N. Basov, and I. K. Schuller, Electrically induced multiple metal-insulator transitions in oxide nanodevices, Physical Review Applied **8**, 054041 (2017).

[13] J. Jeong, N. Aetukuri, T. Graf, T. D. Schladt, M. G. Samant, and S. S. Parkin, Suppression of metal-insulator transition in VO_2 by electric field–induced oxygen vacancy formation, Science **339**, 1402 (2013).

[14] J. Zhang and R. D. Averitt, Dynamics and control in complex transition metal oxides, Annual Review of Materials Research **44**, 19 (2014).

[15] E. Abreu, D. Meyers, V. K. Thorsmølle, J. Zhang, X. Liu, K. Geng, J. Chakhalian, and R. D. Averitt, Nucleation and growth bottleneck in the conductivity recovery dynamics of nickelate ultrathin films, Nano letters **20**, 7422 (2020).

[16] V. A. Stoica, D. Puggioni, J. Zhang, R. Singla, G. L. Dakovski, G. Coslovich, M. H. Seaberg, M. Kareev, S. Middey, P. Kissin, *et al.*, Magnetic order driven ultrafast phase transition in $NdNiO_3$, Physical Review B **106**, 165104 (2022).

[17] S. Catalano, M. Gibert, V. Bisogni, F. He, R. Sutarto, M. Viret, P. Zubko, R. Scherwitzl, G. A. Sawatzky, T. Schmitt, *et al.*, Tailoring the electronic transitions of $NdNiO_3$ films through $(111)_{pc}$ oriented interfaces, APL Materials **3**, 062506 (2015).

[18] J. B. Torrance, P. Lacorre, A. I. Nazzal, E. J. Ansaldo, and C. Niedermayer, Systematic study of insulator-metal transitions in perovskites $RNiO_3$ (R=Pr,Nd,Sm,Eu) due to closing of charge-transfer gap, Physical Review B **45**, 8209 (1992).

[19] U. Staub, G. Meijer, F. Fauth, R. Allenspach, J. Bednorz, J. Karpinski, S. Kazakov, L. Paolasini, and F. d'Acapito, Direct observation of charge order in an epitaxial ndnio 3 film, Physical Review Letters **88**, 126402 (2002).

[20] García-Muñoz, J. L. and Aranda, M. A. G. and Alonso, J. A. and Martínez-Lope, M. J., Structure and charge order in the antiferromagnetic band-insulating phase of $NdNiO_3$, Phys. Rev. B **79**, 134432 (2009).

[21] P. Ruello, B. Perrin, T. Pézeril, V. Gusev, S. Gougeon, N. Chigarev, P. Laffez, P. Picart, D. Mounier, and J. Breteau, Optoacoustical spectrum of the metal–insulator transition compound $NdNiO_3$: Subpicosecond pump–probe study, Physica B: Condensed Matter **363**, 43 (2005).

[22] P. Ruello, S. Zhang, P. Laffez, B. Perrin, and V. Gusev, Ultrafast electronic dynamics in the metal-insulator transition compound $NdNiO_3$, Physical Review B **76**, 165107 (2007).

[23] P. Ruello, S. Zhang, P. Laffez, B. Perrin, and V. Gusev, Laser-induced coherent acoustical phonons mechanisms in the metal-insulator transition compound $NdNiO_3$: Thermal and nonthermal processes, Physical Review B **79**, 094303 (2009).

[24] V. Esposito, L. Rettig, E. M. Bothschafter, Y. Deng, C. Dornes, L. Huber, T. Huber, G. Ingold, Y. Inubushi, T. Katayama, *et al.*, Dynamics of the photoinduced insulator-to-metal transition in a nickelate film, Structural Dynamics **5**, 064501 (2018).

[25] A. D. Caviglia, R. Scherwitzl, P. Popovich, W. Hu, H. Bromberger, R. Singla, M. Mitrano, M. C. Hoffmann, S. Kaiser, P. Zubko, *et al.*, Ultrafast strain engineering in complex oxide heterostructures, Physical Review Letters **108**, 136801 (2012).

[26] A. D. Caviglia, M. Först, R. Scherwitzl, V. Khanna, H. Bromberger, R. Mankowsky, R. Singla, Y.-D. Chuang, W. S. Lee, O. Krupin, *et al.*, Photoinduced melting of magnetic order in the correlated electron insulator $NdNiO_3$, Physical Review B **88**, 220401 (2013).

[27] M. Först, A. Caviglia, R. Scherwitzl, R. Mankowsky, P. Zubko, V. Khanna, H. Bromberger, S. Wilkins, Y.-D. Chuang, W. Lee, *et al.*, Spatially resolved ultrafast magnetic dynamics initiated at a complex oxide heterointerface, Nature Materials **14**, 883 (2015).

[28] M. Först, K. R. Beyerlein, R. Mankowsky, W. Hu, G. Mattoni, S. Catalano, M. Gibert, O. Yefanov, J. N. Clark, A. Frano, *et al.*, Multiple supersonic phase fronts launched at a complex-oxide heterointerface, Physical Review Letters **118**, 027401 (2017).

[29] B. Torriss, J. Margot, and M. Chaker, Metal-insulator transition of strained $SmNiO_3$ thin films: Structural, electrical and optical properties, Scientific Reports **7**, 1 (2017).

[30] N. Shukla, T. Joshi, S. Dasgupta, P. Borisov, D. Lederman, and S. Datta, Electrically induced insulator to metal transition in epitaxial $SmNiO_3$ thin films, Applied Physics Letters **105**, 012108 (2014).

[31] See Supplemental Material at url for sample XRD and resistivity data, exponential fits, (002) Bragg peak FWHM and integrated intensity trends for all fluences, half order peak data, laser induced heating calculation, thermal transport calculation, Poisson expansion calculation, which includes Refs. [32-35, 40].

[32] M. Stewart, J. Liu, M. Kareev, J. Chakhalian, and D. Basov, Mott physics near the insulator-to-metal transition in $NdNiO_3$, Physical Review Letters **107**, 176401 (2011).

[33] V. Barbeta, R. Jardim, M. Torikachvili, M. Escote, F. Cordero, F. Pontes, and F. Trequattrini, Metal-insulator transition in $Nd_{1-x}Eu_xNiO_3$ probed by specific heat and anelastic measurements, Journal of Applied Physics **109**, 07E115 (2011).

[34] J. Pérez-Cacho, J. Blasco, J. García, M. Castro, and J. Stankiewicz, Study of the phase transitions in $SmNiO_3$, Journal of Physics: Condensed Matter **11**, 405 (1999).

[35] M. Hooda and C. Yadav, Electronic properties and the nature of metal–insulator transition in $NdNiO_3$ prepared at ambient oxygen pressure, Physica B: Condensed Matter **491**, 31 (2016).

[36] M. H. Upton, Y. Choi, H. Park, J. Liu, D. Meyers, J. Chakhalian, S. Middey, J.-W. Kim, and P. J. Ryan, Novel electronic behavior driving $NdNiO_3$ metal-insulator transition, Physical Review Letters **115**, 036401 (2015).

[37] I. C. Tung, P. V. Balachandran, J. Liu, B. A. Gray, E. A. Karapetrova, J. H. Lee, J. Chakhalian, M. J. Bedzyk, J. M. Rondinelli, and J. W. Freeland, Connecting bulk symmetry and orbital polarization in strained $RNiO_3$ ultrathin films, Physical Review B **88**, 205112 (2013).

[38] D. Walko, Y.-M. Sheu, M. Trigo, and D. Reis, Thermal transport in thin films measured by time-resolved, grazing incidence x-ray diffraction, Journal of Applied Physics **110**, 102203 (2011).

[39] H. Wen, L. Guo, E. Barnes, J. H. Lee, D. A. Walko, R. D. Schaller, J. A. Moyer, R. Misra, Y. Li, E. M. Dufresne, *et al.*, Structural and electronic recovery pathways of a photoexcited ultrathin VO_2 film, Physical Review B **88**, 165424 (2013).

[40] R. B. Wilson, B. A. Apgar, W.-P. Hsieh, L. W. Martin, and D. G. Cahill, Thermal conductance of strongly bonded metal-oxide interfaces, Physical Review B **91**, 115414 (2015).

[41] R. Li, O. A. Ashour, J. Chen, H. E. Elsayed-Ali, and P. M. Rentzepis, Femtosecond laser induced structural dynamics and melting of Cu (111) single crystal. An ultrafast time-resolved x-ray diffraction study, Journal of Applied Physics **121**, 10.1063/1.4975198 (2017), 055102.

[42] B. Truc, P. Usai, F. Pennacchio, G. Berruto, R. Claude, I. Madan, V. Sala, T. LaGrange, G. M. Vanacore, S. Benhabib, and F. Carbone, Ultrafast generation of hidden phases via energy-tuned electronic photoexcitation in magnetite (2022), arXiv:2210.00070 [cond-mat.str-el].